

# A computationally efficient electrophysiological model of human ventricular cells

O. BERNUS,<sup>1</sup> R. WILDERS,<sup>2</sup> C. W. ZEMLIN,<sup>3</sup> H. VERSCHELDE,<sup>1</sup> AND A. V. PANFILOV<sup>4</sup>

<sup>1</sup>Department of Mathematical Physics and Astronomy, Gent University, 9000 Gent, Belgium;

<sup>2</sup>Department of Physiology, Academic Medical Center, University of Amsterdam, 1105 AZ

Amsterdam; and Department of Medical Physiology, University Medical Center Utrecht, 3584 CG

Utrecht; <sup>3</sup>Institute for Theoretical Biology, Humboldt University, 10115 Berlin, Germany; and

<sup>4</sup>Department of Theoretical Biology, Utrecht University, 3584 CG Utrecht, The Netherlands

Received 14 August 2001; accepted in final form 21 January 2002

**Bernus, O., R. Wilders, C. W. Zemlin, H. Verschelde, and A. V. Panfilov.** A computationally efficient electrophysiological model of human ventricular cells. *Am J Physiol Heart Circ Physiol* 282: H2296–H2308, 2002. First published January 24, 2002; 10.1152/ajpheart.00731.2001.—Recent experimental and theoretical results have stressed the importance of modeling studies of reentrant arrhythmias in cardiac tissue and at the whole heart level. We introduce a six-variable model obtained by a reformulation of the Priebe-Beuckelmann model of a single human ventricular cell. The reformulated model is 4.9 times faster for numerical computations and it is more stable than the original model. It retains the action potential shape at various frequencies, restitution of action potential duration, and restitution of conduction velocity. We were able to reproduce the main properties of epicardial, endocardial, and M cells by modifying selected ionic currents. We performed a simulation study of spiral wave behavior in a two-dimensional sheet of human ventricular tissue and showed that spiral waves have a frequency of 3.3 Hz and a linear core of ~50-mm diameter that rotates with an average frequency of 0.62 rad/s. Simulation results agreed with experimental data. In conclusion, the proposed model is suitable for efficient and accurate studies of reentrant phenomena in human ventricular tissue.

action potential; computer simulation; mathematical model; reentrant arrhythmia; spiral wave

THE HISTORY of modeling biological excitable media such as nerve and heart tissue started 50 years ago with the Hodgkin-Huxley model of the giant squid axon (19). The first model of cardiac tissue (Purkinje fibers) was proposed by Noble in 1962 (30) and consisted of four variables. During the following decades, the experimental techniques for studying the properties of the cell membrane were improved continuously, leading to new cardiac tissue models of increasing accuracy, e.g., the phase-2 Luo-Rudy (LR) model of a single guinea pig ventricular cell (26), which has 12 variables, and the models developed by Noble et al., consisting of 40–60 equations (see, for example, Ref. 31). Recently, comprehensive models have been proposed to account for spe-

cific properties of human cardiac tissue: Nygren et al. (32) and Courtemanche et al. (8) developed models of single human atrial cells, whereas Priebe and Beuckelmann (35) proposed a model of a single human ventricular cell.

The Priebe-Beuckelmann (PB) model is based on the phase-2 LR model. However, five major ionic currents, including the fast ( $I_{Kr}$ ) and slow ( $I_{Ks}$ ) components of the delayed rectifier  $K^+$  current, the L-type  $Ca^{2+}$  current ( $I_{Ca}$ ), the transient outward  $K^+$  current ( $I_{to}$ ), and the inward rectifier  $K^+$  current ( $I_{K1}$ ), are based on experimental data obtained on human myocytes. In addition, parameters of the intracellular  $Ca^{2+}$  concentration ( $[Ca^{2+}]_i$ ) handling were changed in such a way that simulated transients are comparable to observed experimental data on human myocytes (4). The remaining currents have been adjusted from the LR model, with their amplitude scaled to fit human cell data.

Priebe and Beuckelmann developed their model to compare the electrophysiological properties of failing and nonfailing ventricular myocytes. It can be used for accurate simulations of the ionic currents and concentrations in a single cell during electrical activity. Our objective, however, is to simulate reentrant sources of arrhythmias in two (2-D) and three dimensions (3-D), which are believed to underlie most ventricular tachycardias and ventricular fibrillation (18, 21, 43). Although the PB model is based on experimental measurements in human heart tissue, we refrained from using it for the study of reentrant arrhythmias for several reasons. First, the complexity and the high number of variables make the PB model inefficient for extensive computer simulations of large pieces of tissue. Second, the PB model is a “second-generation model” in which, besides membrane potential and gating variables, ion concentrations vary in time. Second-generation models made up of ordinary differential equations describing the time dependence of membrane potential, gating variables, and ion concentrations, are inherently unstable, showing complications

Address for reprint requests and other correspondence: O. Bernus, Dept. of Mathematical Physics and Astronomy, Krijgslaan 281 (S9), 9000 Gent, Belgium (E-mail: olivier.bernus@rug.ac.be).

The costs of publication of this article were defrayed in part by the payment of page charges. The article must therefore be hereby marked “advertisement” in accordance with 18 U.S.C. Section 1734 solely to indicate this fact.

involving long-term drifts of ion concentrations and degeneracy of equilibria, as recently emphasized by both Arce et al. (2) and Endresen and Skarland (12).

A different approach to study reentrant sources of arrhythmias in 2-D and 3-D is using low-dimensional, FitzHugh-Nagumo-type models, e.g., the Fenton-Karma model (14), which allow one to fit some overall tissue properties using three state variables. This approach, however, does not reproduce the shape of the action potential (AP), which is believed to be important for many problems, e.g., in electrocardiography. It also does not permit the study of effects of individual ionic currents on cardiac activation.

The main issue of this paper is the development of a model of an intermediate class. It should be computationally efficient and less complex than the "second-generation" ionic models and free of their inherent instabilities. At the same time, the model should retain important properties of human ventricular tissue such as restitution properties, AP shape, and change of AP shape under variation of major ionic currents. This aim was achieved by reformulating the PB model as a six-variable model, which keeps the major ionic currents but discards some single cell processes that do not substantially affect the desired tissue properties. It should be noted that the reformulation procedure does not depend on the PB model and can be applied to any ionic model.

## MATERIALS AND METHODS

The several stages in the reformulation of the PB model are discussed for each ionic current of the reduced model. We also pay attention to the numerical accuracy and stability of the reduced model and we discuss numerical schemes used in the simulations. Throughout this paper, time is in ms, membrane potential is in mV, ion concentrations are in mM, rate constants are in  $\text{ms}^{-1}$ , current is in pA/pF, and conductance is in nS/pF. Single cell membrane capacitance, cell length, and cell diameter are 153.4 pF, 100  $\mu\text{m}$ , and 22  $\mu\text{m}$ , respectively (same as in the original PB model).

### Reduction of the PB Model

**Intracellular ion concentrations.** The intracellular ion concentration handling in second-generation models can be a source of instabilities (2, 12). This also holds for the PB model, which shows long term drifts of intracellular  $\text{K}^+$  concentration ( $[\text{K}^+]_i$ ) and intracellular  $\text{Na}^+$  concentration ( $[\text{Na}^+]_i$ ) when paced at different frequencies (see *Stability, Ionic Drift and Computational Efficiency*). Therefore, noting that the variations of  $[\text{K}^+]_i$  and  $[\text{Na}^+]_i$  over the course of an AP are extremely small, we set  $[\text{K}^+]_i$  and  $[\text{Na}^+]_i$  to constant values of 140 and 10 mM, respectively, i.e., the initial values in the PB model.

In contrast,  $[\text{Ca}^{2+}]_i$  undergoes substantial changes during the AP. We did not intend to study the details of  $\text{Ca}^{2+}$  dynamics but were mainly interested in the overall properties of  $I_{\text{Ca}}$  and its influence on the AP shape and restitution properties of cardiac tissue. Moreover, in the PB model, the calcium subsystem is represented by a model that mimics  $\text{Ca}^{2+}$ -induced  $\text{Ca}^{2+}$  release as an all-or-none event and reproduces  $\text{Ca}^{2+}$  transients with realistic amplitudes but is phenomenological in construction and is not sufficient to accommodate predictions of intracellular  $\text{Ca}^{2+}$  dynamics un-

der more complex experimental conditions. Therefore, we decided to assign a constant value of 400 nM to the free  $[\text{Ca}^{2+}]_i$  appearing in the  $\text{Ca}^{2+}$  current equations of the original PB model, as an average of its value during the course of an AP. It should be noted that we do not claim that the intracellular calcium handling is irrelevant for cardiac activity but that the simplified equations for  $I_{\text{Ca}}$  listed below are sufficient for a correct representation of AP shape and restitution of AP duration (APD).

**Ionic currents.** **FAST  $\text{Na}^+$  CURRENT.** In the PB model, the kinetic behavior of the fast  $\text{Na}^+$  current ( $I_{\text{Na}}$ ) is described by the very fast activation variable  $m$  and the fast and slow inactivation variables  $h$  and  $j$ , respectively

$$I_{\text{Na}}^o = g_{\text{Na}} \cdot m^3 \cdot h \cdot j \cdot (V_m - E_{\text{Na}}) \quad (1)$$

where the superscript  $o$  denotes an equation used in the original PB model,  $V_m$  is the membrane potential,  $g_{\text{Na}}$  is the maximum sodium conductance, and  $E_{\text{Na}}$  is the Nernst potential (similar notations are used in the equations for the other currents; i.e.,  $g$  is conductance and  $E$  is potential).

The activation of  $I_{\text{Na}}$  is the fastest process during an AP. Hence it is tempting to eliminate  $m$  adiabatically. However, such reduction induces an unrealistically steep upstroke of the AP and drastically decreases the numerical accuracy of the model (see below). Therefore, we refrained from changing  $I_{\text{Na}}$  activation.

Inactivation of  $I_{\text{Na}}^o$  is modeled by the product of two variables,  $h$  and  $j$ . For our purposes, a single variable  $v$  of the Hodgkin-Huxley type (19) suffices. Retaining the quadratic dependence of  $\text{Na}^+$  current inactivation, we obtain

$$I_{\text{Na}} = g_{\text{Na}} \cdot m^3 \cdot v^2 \cdot (V_m - E_{\text{Na}}) \quad (2)$$

The time course of  $v$  is determined by

$$dv/dt = [v_\infty(V_m) - v]/\tau_v(V_m) \quad (3)$$

where  $t$  is time and  $\tau$  is the time constant of relaxation. The constraint we put on  $v$  is that the voltage-clamp behavior of  $I_{\text{Na}}^o$  should be well reproduced by the above-formulated  $I_{\text{Na}}$ . Thus our aim was to obtain a reasonable approximation of  $I_{\text{Na}}^o(t)$  at all times for each clamped potential. The kinetics of the gating variable  $v$  can be determined in two steps. First, we determine  $v_\infty(V_m)$ , which is readily found from *Eqs. 1* and 2

$$v_\infty(V_m) = [h_\infty(V_m) \cdot j_\infty(V_m)]^{1/2} \quad (4)$$

Next, we determine  $\tau_v(V_m)$  by simulating a voltage-clamp experiment and investigating the time course of  $I_{\text{Na}}$  at fixed membrane potentials over a time interval  $[0, T_e]$ . To obtain a reasonable fit for all  $t$ , we used a least-squares method by minimizing the function  $\Delta_{\text{Na}}[\tau_v(V_m)]$ , given by

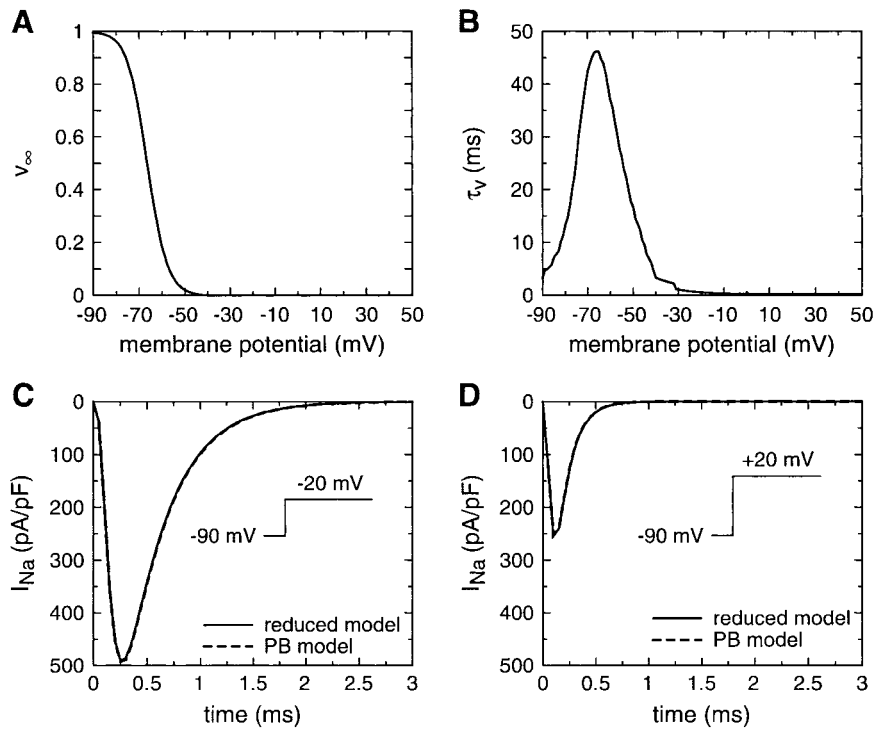
$$\Delta_{\text{Na}}[\tau_v(V_m)] = \int_0^{T_e} [I_{\text{Na}}^o(t) - I_{\text{Na}}(t)]^2 dt \quad (5)$$

Because the  $\text{Na}^+$  current is a rapid current, we performed a voltage clamp during  $T_e = 100$  ms for 10,000 equidistant values of membrane potential within the interval  $[-100$  mV, 90 mV].

The obtained functions,  $v_\infty(V_m)$  and  $\tau_v(V_m)$ , are shown in Fig. 1, *A* and *B*, respectively. In subsequent simulations, we used values directly tabulated from the voltage-clamp simulations, but they can be well approximated by *Eqs. 16* and *17* (see APPENDIX).

Figure 1, *C* and *D*, shows simulated voltage-clamp records of the original and reformulated  $I_{\text{Na}}$ , illustrating that at both test potentials the two closely match, both in amplitude and

Fig. 1. *A* and *B*: steady-state value  $v_\infty$  (*A*) and the time constant  $\tau_v$  (*B*) of the inactivation gating variable  $v$  of the fast  $\text{Na}^+$  current ( $I_{\text{Na}}$ ) in the reformulated Priebe-Beuckelmann (PB) model. *C* and *D*: comparison of  $I_{\text{Na}}$  in the reduced and the original PB model. Activation of  $I_{\text{Na}}$  in response to a voltage-clamp step from a holding potential of  $-90$  mV to a test potential of  $-15$  mV (*C*) and  $+15$  mV (*D*) is shown.



time. Similar results were obtained at other test potentials between  $-70$  and  $+50$  mV (data not shown).

**$\text{Ca}^{2+}$  CURRENT.** Priebe and Beuckelmann modeled  $I_{\text{Ca}}$  using the Hodgkin-Huxley-type (19) activation and inactivation variables  $d$  and  $f$ . In addition, they introduced  $[\text{Ca}^{2+}]_i$ -dependent inactivation by the  $V_m$ -independent factor  $f_{\text{Ca}}$

$$I_{\text{Ca}}^o = g_{\text{Ca}} \cdot d \cdot f \cdot f_{\text{Ca}}([\text{Ca}^{2+}]_i) \cdot (V_m - E_{\text{Ca}}) \quad (6)$$

$$f_{\text{Ca}}([\text{Ca}^{2+}]_i) = 1/(1 + [\text{Ca}^{2+}]_i/0.0006)$$

The activation of  $I_{\text{Ca}}$  is a fast process. Hence, we eliminated  $d$  adiabatically and obtained

$$I_{\text{Ca}} = g_{\text{Ca}} \cdot d_\infty(V_m) \cdot f \cdot f_{\text{Ca}} \cdot (V_m - E_{\text{Ca}}) \quad (7)$$

in which  $f_{\text{Ca}}$  has a constant value of 0.6, because  $[\text{Ca}^{2+}]_i$  was set to 400 nM in the reduced model, as set out above.

**TRANSIENT OUTWARD  $\text{K}^+$  CURRENT.** The equation that Priebe and Beuckelmann used for  $I_{\text{to}}$  is as follows

$$I_{\text{to}}^o = g_{\text{to}} \cdot r \cdot t_o \cdot (V_m - E_{\text{to}}) \quad (8)$$

where  $r$  is a very fast activation variable and  $t_o$  is an inactivation variable. Eliminating  $r$  adiabatically yields our reduced current

$$I_{\text{to}} = g_{\text{to}} \cdot r_\infty(V_m) \cdot t_o \cdot (V_m - E_{\text{to}}) \quad (9)$$

where  $g_{\text{to}}$  was increased by 33% (see below).

**DELAYED RECTIFIER  $\text{K}^+$  CURRENT.** In the PB model,  $\text{K}^+$  current ( $I_{\text{K}}$ ) consists of two components,  $I_{\text{Kr}}$  and  $I_{\text{Ks}}$ , each with a single activation variable,  $X_r$  and  $X_s$ , respectively

$$I_{\text{K}}^o = I_{\text{Kr}} + I_{\text{Ks}} = g_{\text{Kr}} \cdot X_r \cdot (1/(1 + \exp[(V_m + 26)/23])) \times (V_m - E_{\text{Kr}}) + g_{\text{Ks}} \cdot X_s^2 \cdot (V_m - E_{\text{Ks}}) \quad (10)$$

Using the same approach as for  $I_{\text{Na}}$  but with  $T_e$  set to 300 ms, we combined  $I_{\text{Kr}}$  and  $I_{\text{Ks}}$  into a single  $I_{\text{K}}$  with a single activation variable  $X$  and reversal potential  $E_{\text{K}}$  for given  $g_{\text{Kr}}$  and  $g_{\text{Ks}}$

$$I_{\text{K}} = g_{\text{K}} \cdot X^2 \cdot (V_m - E_{\text{K}}) \quad (11)$$

For the parameter values of the original PB model, the resulting  $X_\infty$  and  $\tau_X$  are plotted in Fig. 2, *A* and *B*, respectively. Continuous approximations are listed in the APPENDIX as *Eqs. 34–36*. The value of  $g_{\text{K}}$  was determined by the constraint that  $X_\infty$  should range between 0 and 1. To obtain good restitution of APD, we increased  $\tau_X$  slightly around the resting potential by adding a sigmoidal function  $\tau'_X$  (see the APPENDIX). This minor change had no marked influence on the shape of the AP or on the time course of  $I_{\text{K}}$  (data not shown). Note that using a single  $I_{\text{K}}$  does not prevent our model to be applied for, e.g., studies of drug action on the separate rapid and slow components of the  $\text{K}^+$  current. Therefore, one should just reapply the above fitting procedure with different initial values of  $g_{\text{Kr}}$  and  $g_{\text{Ks}}$  (see RESULTS).

Figure 2, *C* and *D*, shows simulated voltage-clamp records of the original (sum of  $I_{\text{Kr}}$  and  $I_{\text{Ks}}$ ) and reformulated  $I_{\text{K}}$ . In the reformulated model,  $I_{\text{K}}$  shows slightly faster kinetics than in the original PB model, resulting in a somewhat larger current at the end of the 300-ms pulse.

**TIME-INDEPENDENT CURRENTS.** For each of the time-independent currents except  $I_{\text{K1}}$ , we used the original equations from the PB model, which appear in the APPENDIX as *Eqs. 43–50*. For  $I_{\text{K1}}$ , we used the original *Eqs. 39–42* (see the APPENDIX) but increased its conductance ( $g_{\text{K1}}$ ) by 56% (see below).

**PARAMETER VALUES.** The differences between the parameter values of the original PB model and our reduced model have all been listed above. We did not change any of the other parameters. The values of all parameters of the two models are compared in Table 1.

### Numerical Approach

**Mathematical model of wave propagation.** The propagation of an AP is modeled by the (2-D) cable equation as follows

$$C_m \partial V_m / \partial t = -I_{\text{ion}} + (\rho_x \cdot S)^{-1} \partial^2 V_m / \partial x^2 + (\rho_y \cdot S)^{-1} \partial^2 V_m / \partial y^2 \quad (12)$$

$$I_{\text{ion}} = I_{\text{Na}} + I_{\text{Ca}} + I_{\text{to}} + I_{\text{K}} + I_{\text{K1}} + I_{\text{Na,b}} + I_{\text{Ca,b}} + I_{\text{NaK}} + I_{\text{NaCa}}$$

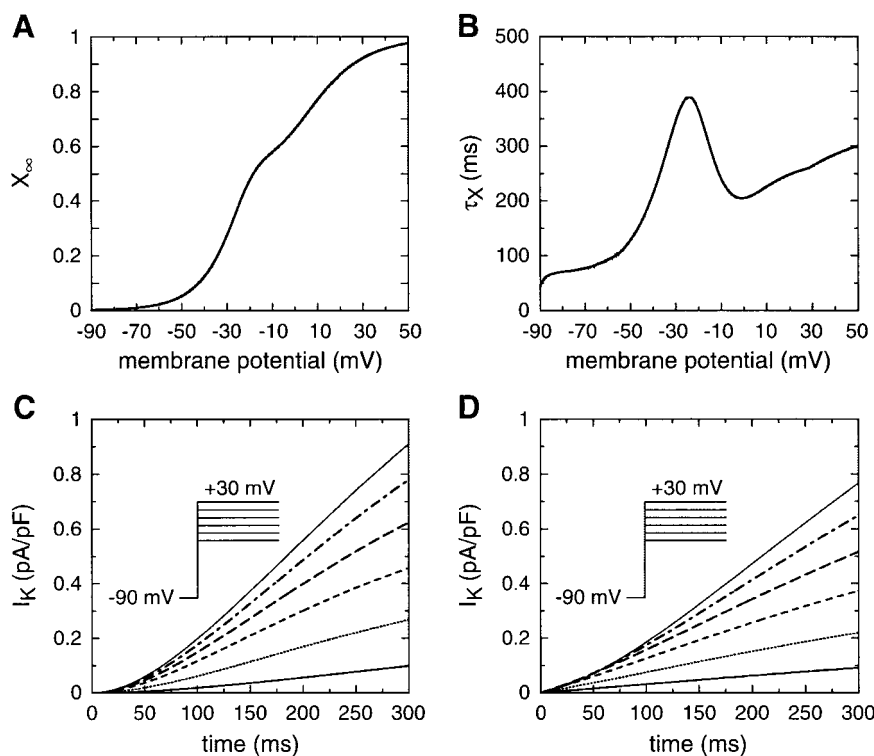


Fig. 2. *A* and *B*: steady-state value  $X_\infty$  (*A*) and time constant  $\tau_X$  (*B*) of the activation variable  $X$  of the delayed rectifier  $K^+$  current ( $I_K$ ) in the reformulated PB model. *C* and *D*: comparison of  $I_K$  in the reduced and the original PB model. Activation of  $I_K$  in response to a voltage-clamp step from a holding potential of  $-90$  mV to a series of test potentials of  $-20$ ,  $-10$ ,  $0$ ,  $+10$ ,  $+20$ , and  $+30$  mV is shown. *C*: reformulated model; *D*: original PB model.

where  $C_m$  is the cell capacitance per surface unit,  $S$  is the surface-to-volume ratio, and  $\rho$  is the cellular resistivity.  $I_{ion}$  is the net membrane current, which consists of the aforementioned  $I_{Na}$ ,  $I_{Ca}$ ,  $I_{to}$ ,  $I_K$ , and  $I_{K1}$  as well as background  $Na^+$  and

Table 1. Parameter values of the PB model and the reduced model

	PB Model	Reduced Model
T, °C	37	37
$g_{Na}$ , nS/pF	16.0	16.0
$g_{Ca}$ , nS/pF	0.064	0.064
$g_{to}$ , nS/pF*	0.3	0.4
$g_K$ , nS/pF*		0.019
$g_{Kr}$ , nS/pF	0.015	
$g_{Ks}$ , nS/pF	0.02	
$g_{K1}$ , nS/pF	2.5	3.9
$g_{Na,b}$ , nS/pF	0.001	0.001
$g_{Ca,b}$ , nS/pF	0.00085	0.00085
$g_{NaK}$ , nS/pF	1.3	1.3
$g_{NaCa}$ , nS/pF	1,000	1,000
$[Ca^{2+}]_i$ , mM	variable	0.0004
$[Ca^{2+}]_e$ , mM	2	2
$[Na^+]_i$ , mM	variable	10
$[Na^+]_e$ , mM	138	138
$[K^+]_i$ , mM	variable	140
$[K^+]_e$ , mM	4	4

PB, Priebe-Beuckelmann; T, temperature;  $g$ , conductances for various currents [fast  $Na^+$  current; ( $g_{Na}$ ),  $Ca^{2+}$  current ( $g_{Ca}$ ), transient outward  $K^+$  current ( $g_{to}$ ),  $K^+$  current ( $g_K$ ), fast component of the  $K^+$  current ( $g_{Kr}$ ), slow component of the  $K^+$  current ( $g_{Ks}$ ), inward rectifier  $K^+$  current ( $g_{K1}$ ), background  $Na^+$  current ( $g_{Na,b}$ ), background  $Ca^{2+}$  current ( $g_{Ca,b}$ ),  $Na^+$ - $K^+$  pump current ( $g_{NaK}$ ), and  $Na^+$ / $Ca^{2+}$  exchanger current ( $g_{NaCa}$ )];  $[Ca^{2+}]_i$  and  $[Ca^{2+}]_e$ , intracellular and extracellular  $Ca^{2+}$  concentrations, respectively;  $[Na^+]_i$  and  $[Na^+]_e$ , intracellular and extracellular  $Na^+$  concentrations, respectively;  $[K^+]_i$  and  $[K^+]_e$ , intracellular and extracellular  $K^+$  concentrations, respectively. \*See Table 4 for  $g_K$  and  $g_{to}$  values for endocardial and M cells.

$Ca^{2+}$  currents ( $I_{Na,b}$  and  $I_{Ca,b}$ , respectively) and the net currents generated by the electrogenic  $Na^+$ - $K^+$  pump and  $Na^+$ / $Ca^{2+}$  exchanger ( $I_{NaK}$  and  $I_{NaCa}$ , respectively). For  $C_m = 2.0 \mu F/cm^2$  and  $S = 0.2 \mu m^{-1}$  (same value as in the PB model) and  $\rho_x = \rho_y = 180 \Omega \cdot cm$  (isotropic case), we obtained a plane wave conduction velocity (CV) of 70 cm/s. The value was the same as that reported by Jongsma and Wilders (22) for longitudinal CV in a linear cable of PB model cells at  $\rho = 181 \Omega \cdot cm$ .

In the one-dimensional case (no derivative with respect to  $y$ ) we used the Crank-Nicholson as well as forward Euler methods to integrate (Eq. 12). In the 2-D case, we used the operator-splitting method to split Eq. 12 into an ordinary differential equation (ODE) for reaction and a partial differential equation (PDE) for diffusion. The PDE was solved using an alternating-direction implicit scheme (34), whereas for the ODE we used a time-adaptive forward Euler scheme with two possible time steps,  $\Delta t_{min} = 0.02$  ms and  $\Delta t_{max} = 0.1$  ms. In this scheme, for each point of the medium, the ODE is solved with  $\Delta t_{max}$ ; if  $dV_m/dt \leq 1$  V/s, we move on to the next point; otherwise, we integrate the ODE at that point five times with  $\Delta t_{min}$  from its initial value. The relaxation equations for the gating variables were integrated using techniques presented by Rush and Larsen (39). All simulations were coded in C++ and run either on a PC with an Intel Pentium III 500-MHz CPU or on a Compaq AlphaServer DS20E with a 666-MHz Alpha 21264 CPU.

**Numerical accuracy.** We tested the numerical accuracy of our model in a cable by changing the time and space step and measuring the CV of a propagating AP. We used a Crank-Nicholson method as well as a forward Euler method, yielding similar results (data not shown). Table 2 shows the results we obtained. In both the original and reduced model, an increase of the time step from 0.01 to 0.02 ms caused a change of  $<1\%$ , whereas an increase in  $\Delta x$  from 0.01 to 0.03 cm reduced CV by 10% [comparable to results obtained by Qu et al. (37)]. Table 2 also show the accuracy of the reduced

Table 2. Numerical accuracy of conduction velocity for different integration time and space steps

	Conduction Velocity, cm/s				
	$\Delta x = 0.10$ mm	$\Delta x = 0.15$ mm	$\Delta x = 0.20$ mm	$\Delta x = 0.25$ mm	$\Delta x = 0.30$ mm
PB model					
$\Delta t = 0.01$ ms	69.4	67.9	65.8	63.4	60.8
$\Delta t = 0.02$ ms	69.5	68.1	65.8	63.4	61.0
Reduced model					
$\Delta t = 0.01$ ms	69.9	68.1	66.0	63.5	60.5
$\Delta t = 0.02$ ms	70.4	68.2	65.8	63.5	60.3
Reduced model with $m = m_\infty$					
$\Delta t = 0.01$ ms	57.1	46.3	38.2	31.7	26.6
$\Delta t = 0.02$ ms	57.4	46.6	38.1	31.7	26.6

$m$ , fast inactivation variable;  $t$ , time;  $x$ , space.

model upon adiabatical elimination of  $m$ . The  $>50\%$  decrease in CV that occurred when  $\Delta x$  was increased from 0.01 to 0.03 cm readily explains why we refrained from eliminating  $m$  adiabatically.

**Restitution of APD and CV.** Restitution of APD was obtained using an S1-S2 protocol on a single cell, consisting of 10 S1 stimuli at 1-Hz frequency and an extrastimulus delivered at some diastolic interval (DI) after the last S1 AP. The restitution curve was then obtained by plotting the APD of the extra AP versus DI. Stimulus current lasted 2 ms, and its strength was two times threshold. The APD was defined using a threshold potential of  $-76$  mV, corresponding to 90% repolarization.

Restitution of CV was measured by periodically pacing one end of a one-dimensional cable of cells. The CV was measured at a point in the middle, and, by increasing the pacing rate, we were able to measure CV at various DIs. Simulations were performed using Crank-Nicholson integration in a cable of 4-cm length with  $\Delta x = 0.10$  mm and  $\Delta t = 0.02$  ms.

**Spiral waves and electrograms.** We obtained spiral waves in a 2-D sheet of ventricular tissue using an S1-S2 protocol. We first paced one side of the tissue (S1), producing a plane wave propagating in one direction. When the refractory tail of this wave crossed the middle of the medium, we moved our pacing electrode to that site and applied a single stimulus (S2) parallel to the S1 wavefront but not over the whole width of the medium. Stimulus currents lasted for 2 (S1) and 5 ms (S2), and their strength was two times threshold for both. The S2 wave front curled around its free end and produced a spiral wave. We calculated the trajectory of the spiral tip using an algorithm presented by Fenton and Karma (14) along an isopotential line of  $-60$  mV.

We simulated electrograms of the spiral wave activity in 2-D by calculating the dipole source density of the membrane potential  $V_m$  in each element, assuming an infinite volume conductor (33). We recorded the electrogram with a single electrode located 10 cm above the center of the sheet of ventricular tissue.

## RESULTS

### AP and Main Ionic Currents

Figure 3 shows a steady-state AP and the main (gated) ionic currents in the reduced and original PB models (solid and dotted lines, respectively) obtained by pacing a single cell at 1 Hz with a 2-ms, 3-nA depolarizing current. The AP in the reduced model is almost identical to the AP in the original model (Fig. 3A and Table 3). We observed an almost perfect match

between  $I_{Na}$  in reduced and original models (Fig. 3B). Peak  $I_{Ca}$  increased by 40%, but the global time course was preserved (Fig. 3C). The time course and amplitude of  $I_K$  were similar in the reduced and original models (Fig. 3D). In the reduced model,  $I_{to}$  shows a significantly larger peak and an earlier inactivation compared with the original model (Fig. 3E). However, the net charge carried by this current in the reduced model only increased by  $\sim 40\%$  compared with the original model (data not shown). Except for the large amplitude of  $I_{to}$  (see below), the AP and ionic currents in the reduced model agreed well with those in the PB

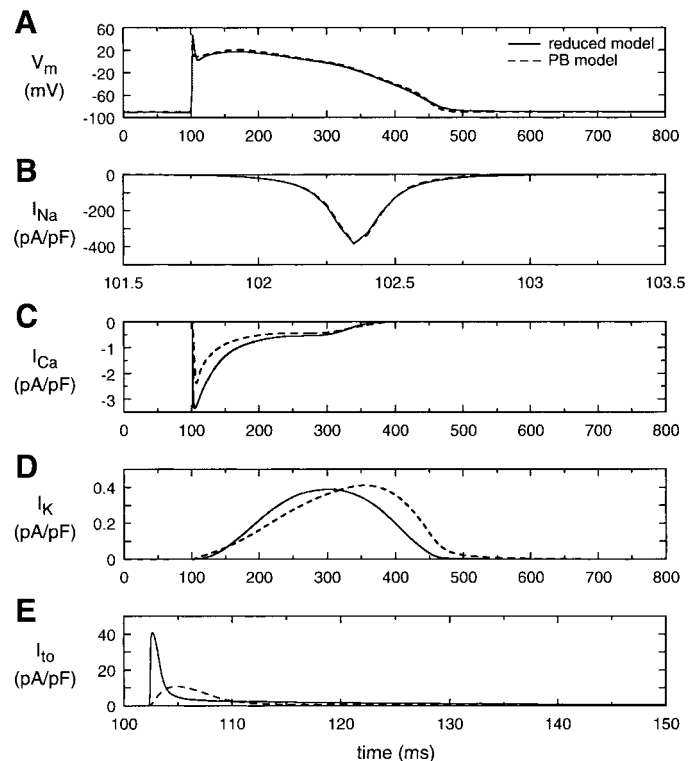


Fig. 3. Action potential (AP) and associated membrane currents in the reformulated PB model and in the original PB model. The AP shown is the fifth from a cell paced at 1 Hz with a 2-ms stimulus current of two times threshold. A: membrane potential ( $V_m$ ); B:  $I_{Na}$ ; C: L-type  $Ca^{2+}$  current ( $I_{Ca}$ ); D:  $I_K$ ; E: transient outward  $K^+$  current ( $I_{to}$ ).

Table 3. Action potential parameters of the PB model and the reduced model

	PB Model	Reduced Model
RMP, mV	-91.2	-90.2
Activation threshold, mV	-60.8	-60.2
$\dot{V}_{\max}$ , V/s	385.2	386.2
APD <sub>50</sub> , ms	251.1	254.0
APD <sub>90</sub> , ms	356.9	357.2

RMP, resting membrane potential;  $\dot{V}_{\max}$ , maximum upstroke velocity; APD<sub>50</sub>, action potential duration at 50% repolarization; APD<sub>90</sub>, action potential duration at 90% repolarization.

model. Moreover, we investigated the relative influence of each gated current on the AP shape by gradually decreasing the conductances and obtained results that closely match those obtained by Priebe and Beuckelmann (35) for the full model (data not shown).

#### Restitution of APD

The APD restitution is known to play a crucial role in the formation and stability of reentrant wave patterns like spiral waves (17, 37). Figure 4A shows the APD restitution curves of the reduced model and the original model as well as the experimental data obtained from the human right ventricle by Morgan et al. (29). The two model curves are quite similar; the reduced model matching the experimental data even slightly better than the original model. Figure 4, B and C, illustrates the changes in shape of the AP with decreasing DI. At short DI, we observed a lowering of the plateau in both models. We conclude that the restitution properties of the PB model are well reproduced in our reduced model, both with respect to AP shape and APD, and that the reformulated model nicely reproduces available experimental data.

#### Restitution of CV

The activation properties of the original PB model and our reduced model are compared in Fig. 5. Figure 5A shows the stimulus strength-duration curves of both models, whereas Fig. 5B shows the CV restitution curves of the PB model. The decrease in CV with decreasing DI is due to the decreasing amount of  $I_{Na}$  that is available for (re)activation. In the full model, this amount is determined by the fast and slow inactivation variables  $h$  and  $j$ , whereas in our model it is solely determined by  $v$ . The curves behave similarly at long DI, but at short DI the reduced model shows a slightly steeper dependence than the original model, caused mainly by  $\tau_v$  being slightly "too small." We did not try to get a perfect match with the CV restitution curve in the full model, because there exist no reliable experimental data on CV restitution in normal human ventricular tissue. Note, however, that the CV restitution properties can easily be adapted to new experimental data by minor modifications of  $\tau_v(V_m)$ .

#### AP Heterogeneity

The transmural heterogeneity of the ventricular AP that has been observed in animal and human myocar-

dium (1, 24, 25, 27) plays an important role in the electrocardiogram (ECG) transcription, especially with respect to the J and T wave. As we intend to investigate and simulate ECGs of ventricular arrhythmias, it is

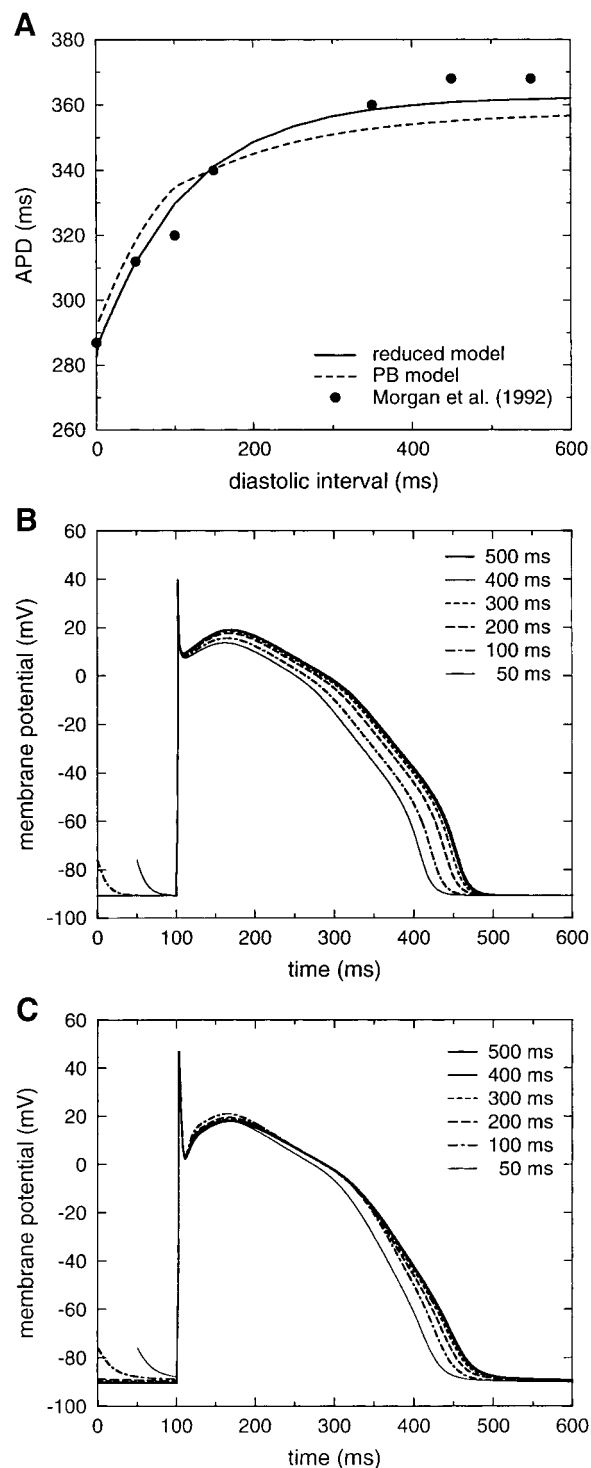


Fig. 4. Restitution of the AP duration (APD). A: APD restitution curves in the reformulated model, original PB model, and experimental data obtained by Morgan et al. (29). B and C: dependence of AP shape on diastolic interval (DI). DI was gradually decreased from 500 to 50 ms, as indicated. B: reformulated model; C: original PB model.

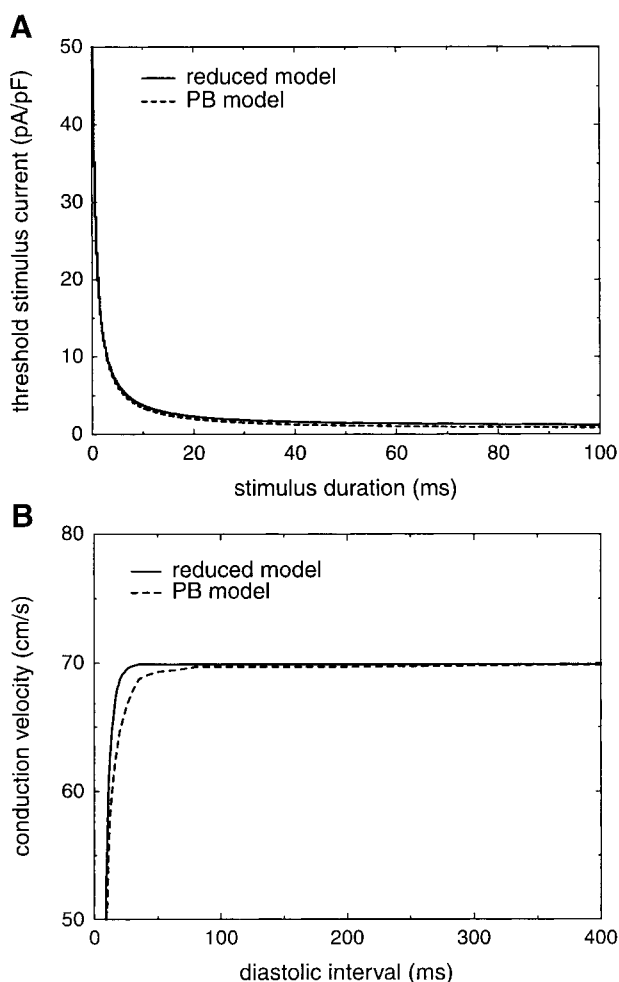


Fig. 5. Activation properties of the reformulated model and original PB model. A: stimulus strength-duration curves; B: conduction velocity restitution curves.

important to take this heterogeneity into account. Three main AP morphologies are observed through the ventricular wall: the epicardial AP with the typical notch and spike-and-dome shape, the M cell AP with a less pronounced notch and prolonged repolarization phase, and the endocardial AP with a more triangular shape (1, 24, 25). The prolonged APD of the M cells is associated with a reduced  $I_{Ks}$  (25), whereas the change from a spike-and-dome to a more triangular shape is due to a transmural gradient in the amplitude and kinetics of  $I_{to}$ . From epicardium to endocardium,  $I_{to}$  shows a decrease in amplitude, a negative shift in half-inactivation voltage ( $V_{shift}$ ), and an increase in reactivation time (24).

As a test on the role of selected ionic currents, we investigated how the reformulated model could reproduce the observed AP heterogeneity. The full PB model and our reduced version thereof show a clear notch and spike-and-dome morphology and were assumed to resemble an epicardial cell. To create an M cell model, we changed both  $I_{to}$  and  $I_K$  (through its slow component  $I_{Ks}$ ). To create an endocardial cell model, we only made changes to  $I_{to}$ .

The amplitude of  $I_{to}$  was changed by altering  $g_{to}$ . We increased the inactivation time of  $I_{to}$  by multiplying the gating functions  $\alpha_{to}(V_m)$  and  $\beta_{to}(V_m)$  with a constant factor of  $p < 1$ , thus increasing  $\tau_{to}$  while preserving the function  $t_{o\infty}$ . The half-inactivation voltage was changed through a shift in the gating functions of  $to$  by  $V_{shift}$ . The resulting equations for  $\tau_{to}(V_m)$  and  $t_{o\infty}(V_m)$  are listed in the APPENDIX as Eqs. 31 and 32. To prolong the APD of the M cells, we decreased  $g_{Ks}$  by 50% in the original PB model and performed new voltage-clamp simulations on the sum of  $I_{Kr}$  and  $I_{Ks}$  to obtain  $X_\infty$ ,  $\tau_X$ , and  $g_K$  for the M cell. The thus-obtained tabulated values of  $X_\infty$  and  $\tau_X$  are well approximated by the functions listed in the APPENDIX as Eqs. 37 and 38. The new  $g_K$  was found to equal 0.013 nS/pF.

The AP heterogeneity was obtained by using the parameter values listed in Table 4. Note that all relative changes are well within the experimentally observed range (24). The simulated APs for epicardium, M cells, and endocardium are shown in Fig. 6, A–C, and have a duration of 360, 362, and 400 ms, respectively, and are similar to the APs observed experimentally (1, 24). Figure 6D shows the APD restitution curves for the different cell types. Like those reported by Antzelevitch et al. (1), the restitution curves for epicardium and endocardium almost coincide, whereas the restitution curve for the M cells is considerably steeper.

### Spiral Waves

The 2-D simulations were performed on a  $700 \times 700$  square lattice with  $\Delta x = 0.25$  mm. We obtained spiral waves using an S1-S2 stimulation protocol, as described in MATERIALS AND METHODS. The results of this computation are shown in Fig. 7. After application of the S2 stimulus (Fig. 7A), the spiral tip drifts along the refractory tail of the wave (Fig. 7B) before curling back (clockwise) and stabilizing approximately at the middle of the medium (Fig. 7C). Figure 7D shows the trajectory of the tip after stabilization. The tip motion occurs along lines that are ended by a quick turn through  $\sim 180^\circ$ . The linear part of the trajectory rotates counterclockwise in space at an angular velocity of  $\sim 0.62$  rad/s. This tip motion is characteristic of the spiral waves with a linear core observed in experiments on thin slices of myocardium (9) and in the whole heart (11, 16) as well as in mathematical models of cardiac tissue (10, 13).

Figure 8A shows a record of membrane potential in a point far from the spiral core (asterisk in Fig. 7C)

Table 4. Parameter values of the reformulated model for the three ventricular cell types

	Epicardial Cells	M cells	Endocardial Cells
$1/p$	1	1.7	2.8
$V_{shift}$ , mV	0	-4	-12
$g_{to}$ , nS/pF	0.4	0.35	0.13
$g_K$ , nS/pF	0.019	0.013	0.019

$1/p$ , scaling factor for inactivation time constant of the transient outward  $K^+$  current ( $I_{to}$ );  $V_{shift}$ , shift in half-inactivation voltage of  $I_{to}$ .

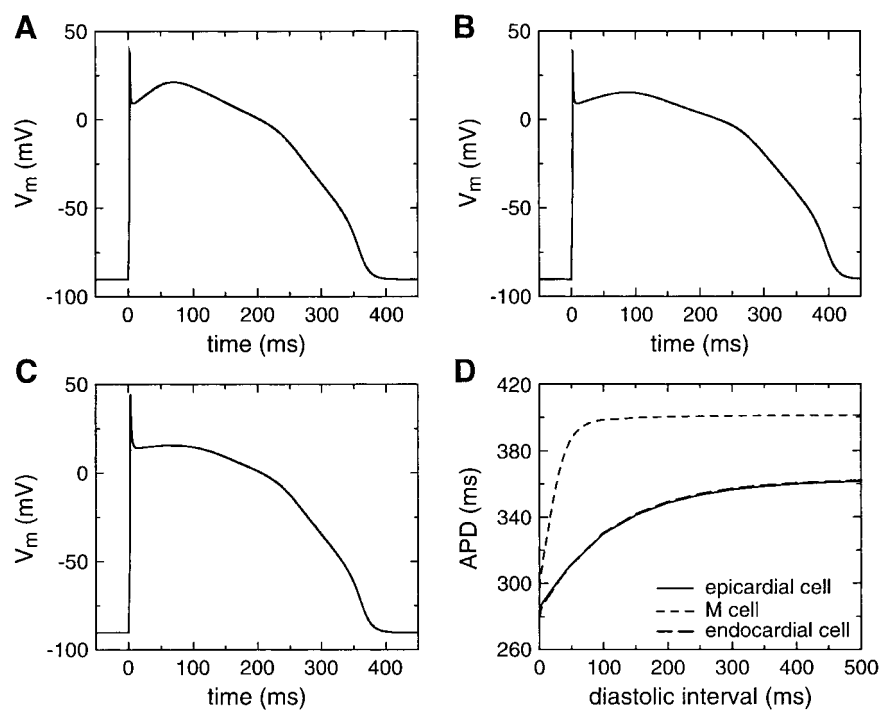
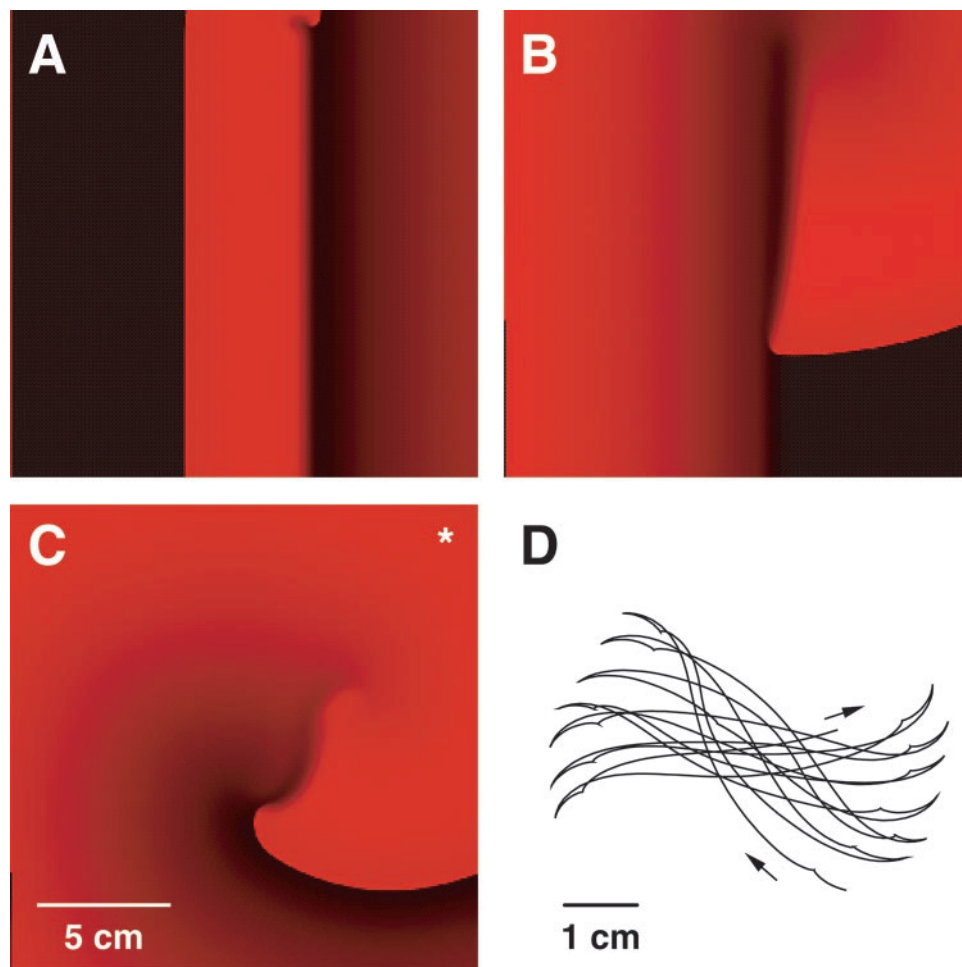


Fig. 6. AP and APD restitution in 3 different configurations of the reformulated model, representing the different cell types that are present in the ventricular wall. A–C: AP of an epicardial cell (A), a midmyocardial cell (M cell) (B), and an endocardial cell (C). D: APD restitution curves for each of the cell types.

Fig. 7. Spiral wave activity in a 2-dimensional (2-D) representation of the reformulated model. A–C: formation of spiral wave by an S1-S2 protocol. D: trajectory of spiral tip during 2 s after stabilization. See text for details.



during 10 s after S1. Due to restitution, the APD changed from  $\sim 350$  to  $\sim 280$  ms. The average period of the spiral wave was  $304.48 \pm 3.09$  ms (means  $\pm$  SD). Figure 8B shows the ECG associated with the spiral wave. It is similar to ECGs obtained during polymorphic ventricular tachycardia. The Fourier transform of the ECG shows a dominant frequency around 3.29 Hz (not shown), which is comparable to the value of  $3.65 \pm 0.46$  Hz obtained in clinical studies (7).

#### Stability, Ionic Drift, and Computational Efficiency

We compared the speed of computations by pacing a cell at 1 Hz during 1,000 s of model time. All computations were performed on the 666-MHz Alpha 21264 CPU of a Compaq AlphaServer DS20E using Euler-type integration with a time step of  $10 \mu\text{s}$ . For the original model, the simulation took 386.5 s of computer time, whereas for the reduced model, the simulation finished in 79.5 s. During this simulation, the original model showed a drift in both  $[\text{Na}^+]_i$  and  $[\text{K}^+]_i$ . Over 1,000 s of model time, mean  $[\text{Na}^+]_i$  decreased from 10 to 8.1 mM (Fig. 9B), whereas the mean  $[\text{K}^+]_i$  decreased nonmonotonically from 140 to 139.5 mM (Fig. 9C). As a consequence, the PB model did not reach a steady state, and, after 1,000 s of model time, the APD ran up to 425 ms (Fig. 9A).

Because  $[\text{Na}^+]_i$  and  $[\text{K}^+]_i$  change very little over the course of one AP, it is tempting to eliminate their drifts by putting them to a constant value. If the above simulation of 1,000 s of model time is repeated with  $[\text{Na}^+]_i$  and  $[\text{K}^+]_i$  set to constant values of 140 and 10 mM, respectively, the PB model reaches a steady state with an APD of  $\sim 360$  ms and the simulation takes 305 s of computer time (data not shown). However, if the cycle length is abruptly changed, e.g., to 2 Hz, a very slow adaptation of  $[\text{Ca}^{2+}]_i$  is observed (Fig. 10B) and it takes  $>1$  min of model time for the cell to reach a new steady state (Fig. 10A).

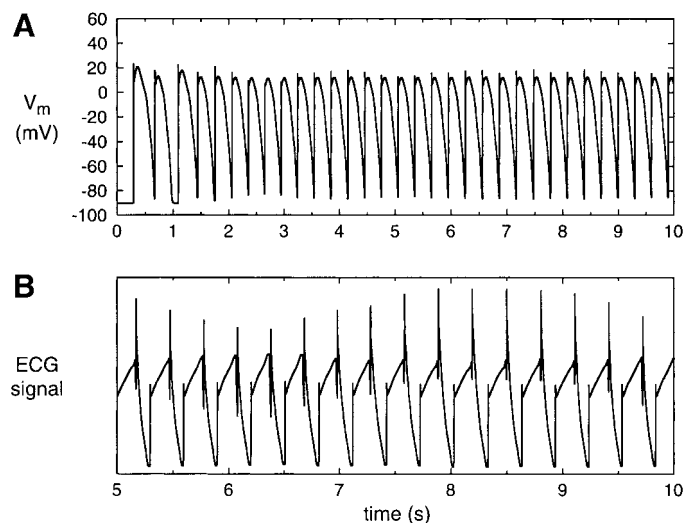


Fig. 8. Membrane potential and electrocardiogram (ECG) during spiral wave activity shown in Fig. 7. Note the different time scales. A:  $V_m$  record at point (650, 650) during 10 s after S1; B: nonscaled ECG ( $time\ 0$  at S1 delivery).

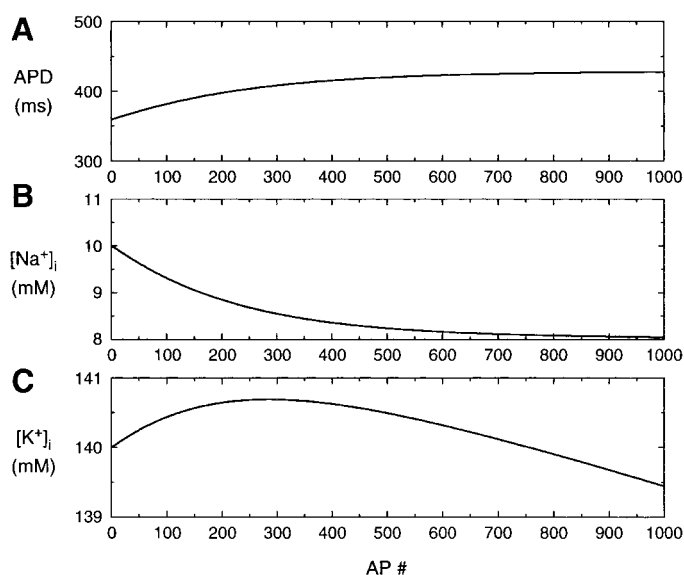


Fig. 9. Beat-to-beat changes in APD (A), mean intracellular  $\text{Na}^+$  concentration ( $[\text{Na}^+]_i$ ; B), and mean intracellular  $\text{K}^+$  concentration ( $[\text{K}^+]_i$ ; C) in the original PB model paced at 1 Hz.

Both these observations are unrealistic because paced isolated cells adapt in a few beats to a given cycle length. They were the main reason why we refrained from using the original PB model, even with  $[\text{Na}^+]_i$  and  $[\text{K}^+]_i$  set to constant values, for extensive simulations of a 2-D spiral wave. In those cases, it would take many rotations before all transient drifts would have disappeared. In the reformulated model, the cell adapts after a few beats to a given cycle length, even after an

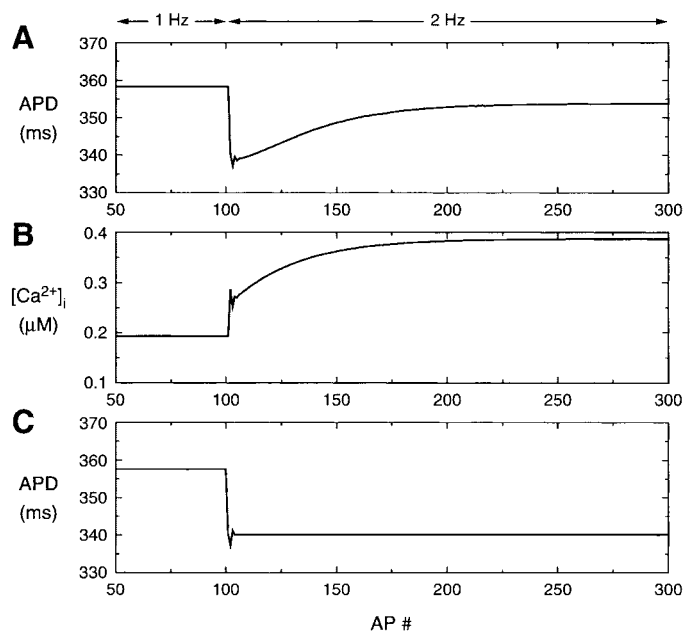


Fig. 10. Beat-to-beat changes in APD (A) and mean intracellular  $\text{Ca}^{2+}$  concentration ( $[\text{Ca}^{2+}]_i$ ; B) in the original PB model ( $[\text{Na}^+]_i$  and  $[\text{K}^+]_i$  fixed at 10 and 140 mM, respectively) upon a step increase in stimulation frequency from 1 to 2 Hz at AP 100. C: beat-to-beat changes in APD in the reformulated model using the same stimulation protocol.

abrupt change (Fig. 10C), just like real isolated cells. Given the increase in computational speed obtained with the reformulated model (an increase by a factor of 4.9 compared with the full PB model and a factor of 3.8 compared with the PB model with constant  $[Na^+]_i$  and  $[K^+]_i$ ) as well as the much faster and more realistic adaptation to changes in cycle length, it is clear that the use of the reduced model saves a huge amount of computational time when investigating reentrant arrhythmias. Also, with the number of model variables reduced from 15 to 6, the demand for computer memory is reduced by a factor of 2.5.

## DISCUSSION

### Action Potential

The results of our simulations show that the overall properties of the AP in the original PB model are well reproduced in the reduced model. The shape of the AP is similar in both models (Fig. 3) and AP parameters are preserved (Table 3). To have comparable resting membrane potential and APD, we had to increase  $g_{K1}$  by 56%. With a maximum outward current in the negative voltage range of 0.36 pA/pF at  $-60$  mV, Beuckelmann et al. (5) found quite low values of  $I_{K1}$  in human ventricular myocytes, whereas higher values, up to 8 pA/pF (23), have been reported in other studies. In our reduced model, with increased  $g_{K1}$ , the maximum of  $I_{K1}$  in the negative voltage range is 1.33 pA/pF, which is well within the range of experimental data.

### Main Gated Currents

The overall time course of the individual ionic currents resembled that in the original model (Fig. 3). The amplitudes of  $I_{to}$  and  $I_{Ca}$  are, however, larger than in the PB model, due to the adiabatic elimination of the activation variables  $r$  and  $d$ , respectively. The amplitude of  $I_{to}$  is furthermore enhanced by a 33% increase in  $g_{to}$ . This increase was necessary to preserve the typical notch that follows the AP upstroke. Although these amplitudes may seem less realistic, we found that they had no influence on the properties of the AP we studied.

### Restitution Properties

The restitution properties of the original PB model were obtained far from steady states, where large ionic drifts occur (see Fig. 9). Therefore, we did not solely compare our model with the original PB model but also with available experimental data. The reformulated model closely fits the data obtained by Morgan et al. (29) (Fig. 4A). Experimental studies of restitution in human myocardium have also shown biphasic restitution curves (15, 28). This phenomenon is still poorly understood and, so far, no ionic models have been developed to reproduce these nonmonotonic curves. Biphasic restitution curves can easily be obtained by introducing a DI dependency of a model parameter (e.g.,  $g_{Ca}$ ) (44). Such approach is, however, detached

from the underlying electrophysiology. Therefore, we decided to wait until more experimental data on this property become available before trying to modify the APD restitution curve.

The CV restitution is steeper than in the full model (Fig. 5B). Because there are no experimental data on CV restitution in human myocardium, we did not attempt to flatten the CV curve in the reduced model. Moreover, when Saumarez et al. (40, 41) measured the latency of propagating pulses in human ventricular tissue, they found that normal ventricular tissue (less susceptible to cardiac arrhythmias) showed a steeper increase in latency at short DI than the tissue of patients who had cardiac arrhythmias. Therefore, the steeper curve in the reduced model may be an even more accurate model of normal ventricular tissue.

### AP Heterogeneity

On the basis of experimental findings on  $I_{to}$  and  $I_{Ks}$  (24, 25), we were able to reproduce the observed AP heterogeneity in ventricular muscle. We obtained an APD prolongation in the M cells through a 50% block of  $I_{Ks}$  like reported by Liu et al. (25). The simulated APD difference between M cells and epicardium and endocardium is, however, smaller than the difference observed by Li et al. (24) in myocytes isolated from the human right ventricle. This could indicate that other currents are involved in the APD prolongation of M cells. Indeed,  $I_{K1}$  seems to be somewhat smaller in M cells from the canine ventricle (25), and transmural inhomogeneities in other currents are starting to be reported as well (3, 45, 46). On the other hand, quite small APD differences were measured in guinea pig ventricular tissue by Main et al. (27). These observations reflect species differences, and, more recently, differences between right and left ventricles have also been observed (42). For the moment, we feel that our simulations of the observed transmural AP heterogeneity, based on differences in  $I_{to}$  and  $I_{Ks}$ , are realistic enough, but we are aware that we may have to include transmural inhomogeneities in other currents as well, once these are demonstrated experimentally in the human ventricle.

### Numerical Efficiency

We were able to reformulate the PB model with five gating variables by altering only two electrophysiological parameters,  $g_{to}$  and  $g_{K1}$ . The total number of variables has been reduced from 15 in the original model to 6 in the reformulated model, i.e., the membrane potential  $V_m$  and the gating variables of  $I_{Na}$  ( $m$  and  $v$ ),  $I_{Ca}$  ( $f$ ),  $I_{to}$  ( $to$ ), and  $I_K$  ( $X$ ). The computational gain at the cellular level was of the order of a factor of four. The computational speed can be increased further by the choice of sophisticated numerical schemes, such as adaptive space masks (6) or adaptive time step schemes (36). We used a scheme similar to the latter in 2-D simulations of reentrant arrhythmias. Furthermore, there was a considerable gain in stability and

rate adaptation. Moreover, in the reduced model, it was less difficult to relate changes in parameter values to changes in the AP. Taken together, the reformulated model is very efficient for extensive 2-D and 3-D simulations of reentrant arrhythmias.

### Spiral Waves in 2-D

The spiral waves generated with the reduced model show meandering dynamics, preceded by a short transient drift, and have a period of  $\sim 300$  ms. The ECG of the 2-D spiral waves is polymorphic and supports the idea that meandering reentrant arrhythmias underlie polymorphic ventricular tachycardias (18, 21, 43). We are aware of the quantitative limitations of 2-D simulations of spiral waves and associated ECGs. The geometry and anisotropy of the ventricles can have an important influence on the dynamics of vortices and the electrical properties of the human body have to be taken into account. The AP heterogeneity addressed above is also important for a correct description of heart repolarization, e.g., in modeling the J and T waves of the ECG. The 2-D spatial domain in which we study spiral waves is quite large compared with the size of the human heart ( $17.5 \times 17.5$  cm). However, our computations show that once a spiral is formed, it can rotate in a medium as small as  $8.2 \times 8.2$  cm. In the whole heart, spiral waves may be formed because of geometry and anisotropy.

### Limitations of the Model

The inherent limitations of the full PB model have been discussed in the paper by Priebe and Beuckelmann (35). The main limitation of our reformulated model is the lack of ionic concentration handling. Giving constant values to all intracellular concentrations is a drastic way of reducing the number of equations and puts some constraints on the applicability of the model; the dynamics of calcium overload, sodium overload, etc., can no longer be studied. It should, however, be noted that the equations representing the calcium subsystem are still evolving and even the latest comprehensive models fail to adequately represent fundamental properties of calcium handling. Jafri et al. (20) incorporated an entirely new description of intracellular  $\text{Ca}^{2+}$  handling into the phase-2 LR model, resulting in a set of as many as 30 ordinary differential equations that provide an improved description of the L-type  $\text{Ca}^{2+}$  channels and  $\text{Ca}^{2+}$ -induced  $\text{Ca}^{2+}$  release from ryanodine receptor channels exhibiting adaptation. Whereas this model reproduces important aspects of cardiac  $\text{Ca}^{2+}$  cycling, it also exhibits all-or-none rather than graded  $\text{Ca}^{2+}$  release (38).

In summary, we developed an efficient electrophysiological model of single human ventricular cells that may facilitate and improve large scale computational studies of reentrant arrhythmias.

## APPENDIX

### MODEL EQUATIONS

#### Equilibrium Potentials

$$E_{\text{Na}} = (RT/F) \ln ([\text{Na}^+]_e / [\text{Na}^+]_i)$$

$$E_{\text{Ca}} = (RT/2F) \ln ([\text{Ca}^{2+}]_e / [\text{Ca}^{2+}]_i)$$

$$E_{\text{to}} = (RT/F) \ln [(0.043 \cdot [\text{Na}^+]_e + [\text{K}^+]_e) / (0.043 \cdot [\text{Na}^+]_i + [\text{K}^+]_i)]$$

$$E_{\text{K}} = (RT/F) \ln ([\text{K}^+]_e / [\text{K}^+]_i)$$

where  $R$  is the universal gas constant,  $T$  is the absolute temperature,  $F$  is the Faraday constant, and  $[\text{Na}^+]_e$ ,  $[\text{Ca}^{2+}]_e$ , and  $[\text{K}^+]_e$  are the extracellular  $\text{Na}^+$ ,  $\text{Ca}^{2+}$ , and  $\text{K}^+$  concentrations, respectively.

#### Inward Currents

##### Fast $\text{Na}^+$ current.

$$I_{\text{Na}} = g_{\text{Na}} \cdot m^3 \cdot v^2 \cdot (V_m - E_{\text{Na}}) \quad (13)$$

$$\alpha_m = [0.32 \cdot (V_m + 47.13)] / \{1 - \exp[-0.1 \cdot (V_m + 47.13)]\} \quad (14)$$

$$\beta_m = 0.08 \cdot \exp(-V_m/11) \quad (15)$$

$$v_\infty = 0.5 \cdot [1 - \tanh(7.74 + 0.12 \cdot V_m)] \quad (16)$$

$$\tau_v = 0.25 + 2.24 \cdot \{[1 - \tanh(7.74 + 0.12 \cdot V_m)] / [1 - \tanh[0.07 \cdot (V_m + 92.4)]]\} \quad (17)$$

##### Slow $\text{Ca}^{2+}$ current.

$$I_{\text{Ca}} = g_{\text{Ca}} \cdot d_\infty \cdot f \cdot f_{\text{Ca}} \cdot (V_m - E_{\text{Ca}}) \quad (18)$$

$$d_\infty = \alpha_d / (\alpha_d + \beta_d) \quad (19)$$

$$\alpha_d = (14.98 \cdot \exp\{-0.5 \times [(V_m - 22.36)/16.68]^2\}) / [16.68 \cdot \sqrt{(2\pi)}] \quad (20)$$

$$\beta_d = 0.1471 - (5.3 \cdot \exp\{-0.5 \times [(V_m - 6.27)/14.93]^2\}) / [14.93 \cdot \sqrt{(2\pi)}] \quad (21)$$

$$\alpha_f = (6.87 \cdot 10^{-3}) / \{1 + \exp[-(6.1546 - V_m)/6.12]\} \quad (22)$$

$$\beta_f = \{0.069 \cdot \exp[-0.11 \cdot (V_m + 9.825)] + 0.011\} / \{1 + \exp[-0.278 \cdot (V_m + 9.825)]\} + 5.75 \cdot 10^{-4} \quad (23)$$

$$f_{\text{Ca}} = 1 / (1 + [\text{Ca}^{2+}]_i / 0.0006) \quad (24)$$

#### Outward Currents

##### Transient outward current.

$$I_{\text{to}} = g_{\text{to}} \cdot r_\infty \cdot t_o \cdot (V_m - E_{\text{to}}) \quad (25)$$

$$r_\infty = \alpha_r / (\alpha_r + \beta_r) \quad (26)$$

$$\alpha_r = \{0.5266 \cdot \exp[-0.0166 \cdot (V_m - 42.2912)]\} / \{1 + \exp[-0.0943 \cdot (V_m - 42.2912)]\} \quad (27)$$

$$\beta_r = \{5.186 \cdot 10^{-5} \cdot V_m + 0.5149 \cdot \exp[-0.1344 \times (V_m - 5.0027)]\} / \{1 + \exp[-0.1344 \times (V_m - 5.186 \cdot 10^{-5})]\} \quad (28)$$

$$\alpha_{t_o} = \{5.612 \cdot 10^{-5} \cdot V_m + 0.0721 \cdot \exp[-0.173 \times (V_m + 34.2531)]\} / \{1 + \exp[-0.1732 \cdot (V_m + 34.2531)]\} \quad (29)$$

$$\beta_{t_o} = \{1.215 \cdot 10^{-4} \cdot V_m + 0.0767 \cdot \exp[-1.66 \cdot 10^{-9} \times (V_m + 34.0235)]\} / \{1 + \exp[-0.1604 \cdot (V_m + 34.0235)]\} \quad (30)$$

$$\tau_{to}(V_m) = 1/[p\alpha_{to}(V_m) + p\beta_{to}(V_m)] \quad (31)$$

$$to_{\infty}(V_m) = \alpha_{to}(V_m - V_{shift})/[\alpha_{to}(V_m - V_{shift}) + \beta_{to}(V_m - V_{shift})] \quad (32)$$

*Delayed rectifier K<sup>+</sup> current.*

$$I_K = g_K \cdot X^2 \cdot (V_m - E_K) \quad (33)$$

For endocardial and epicardial cells

$$X_{\infty} = 0.988/[1 + \exp(-0.861 - 0.0620 \cdot V_m)] \quad (34)$$

$$\tau_X = 240 \cdot \exp[-(25.5 + V_m)^2/156] + 182 \cdot [1 + \tanh(0.154 + 0.0116 \cdot V_m)] + \tau'_X \quad (35)$$

$$\tau'_X = 40 \cdot [1 - \tanh(160 + 2 \cdot V_m)] \quad (36)$$

For M cells

$$X_{\infty} = 0.972/[1 + \exp(-2.036 - 0.0834 \cdot V_m)] \quad (37)$$

$$\tau_X = 380 \cdot \exp[-(25.5 + V_m)^2/156] + 166 \cdot [1 + \tanh(0.558 + 0.0169 \cdot V_m)] \quad (38)$$

*Inward rectifier K<sup>+</sup> current.*

$$I_{K1} = g_{K1} \cdot K1_{\infty} \cdot (V_m - E_K) \quad (39)$$

$$K1_{\infty} = \alpha_{K1}/(\alpha_{K1} + \beta_{K1}) \quad (40)$$

$$\alpha_{K1} = 0.1/[1 + \exp[0.06 \cdot (V_m - E_K - 200)]] \quad (41)$$

$$\beta_{K1} = \{3 \cdot \exp[2 \cdot 10^{-4} \cdot (V_m - E_K + 100)] + \exp[0.1 \cdot (V_m - E_{K1} - 10)]\}/[1 + \exp[-0.5 \cdot (V_m - E_K)]] \quad (42)$$

*Background Currents*

*Ca<sup>2+</sup> background current.*

$$I_{Ca,b} = g_{Ca,b} \cdot (V_m - E_{Ca}) \quad (43)$$

*Na<sup>+</sup> background current.*

$$I_{Na,b} = g_{Na,b} \cdot (V_m - E_{Na}) \quad (44)$$

*Pump and Exchanger Currents*

*Na<sup>+</sup>-K<sup>+</sup> pump.*

$$I_{NaK} = g_{NaK} \cdot f_{NaK} \cdot f'_{NaK} \quad (45)$$

$$f_{NaK} = 1/[1 + 0.1245 \cdot \exp(-0.0037 \cdot V_m) + 0.0365 \cdot \sigma \cdot \exp(-0.037 \cdot V_m)] \quad (46)$$

$$f'_{NaK} = \{1/[1 + (10/[Na^+]_i)^{1.5}]\} \cdot [K^+]_i/[K^+]_e + 1.5 \quad (47)$$

$$\sigma = 0.1428 \cdot [\exp([Na^+]_e/67.3) - 1] \quad (48)$$

*Na<sup>+</sup>/Ca<sup>2+</sup> exchanger.*

$$I_{NaCa} = g_{NaCa} \cdot f_{NaCa} \quad (49)$$

$$f_{NaCa} = (87.5^3 + [Na^+]_e^3)^{-1} \cdot (1.38 + [Ca^{2+}]_e)^{-1} \cdot \{1 + 0.1 \cdot \exp(-0.024 \cdot V_m)\}^{-1} \cdot \{[Na^+]_i^3 \cdot [Ca^{2+}]_e \cdot \exp(0.013 \cdot V_m) - [Na^+]_e^3 \cdot [Ca^{2+}]_i \cdot \exp(-0.024 \cdot V_m)\} \quad (50)$$

We are thankful to Kirsten H. W. J. ten Tusscher for help in 2-D computations and Dr. S. McNab for editorial advice.

This research was supported by a specialization grant from the Flemish Institute for the Promotion of Scientific and Technological Research in Industry and by the Netherlands Organization for Scientific Research via the Research Council for Earth and Life Sciences.

## REFERENCES

1. **Antzelevitch C, Nesterenko VV, Muzikant AL, Rice JJ, Chen G, and Colatsky T.** Influence of transmural repolarization gradients on the electrophysiology and pharmacology of ventricular myocardium. Cellular basis for the Brugada and long QT-syndromes. *Phil Trans R Soc London A* 359: 1201–1216, 2001.
2. **Arce H, Xu A, González H, and Guevara MR.** Alternans and higher-order rhythms in an ionic model of a sheet of ischemic ventricular muscle. *Chaos* 10: 411–426, 2000.
3. **Ashamalla SM, Navarro D, and Ward CA.** Gradient of sodium current across the left ventricular wall of adult rat hearts. *J Physiol (Lond)* 536: 439–443, 2001.
4. **Beuckelmann DJ, Näbauer M, and Erdmann E.** Intracellular calcium handling in isolated ventricular myocytes from patients with terminal heart failure. *Circulation* 85: 1046–1055, 1992.
5. **Beuckelmann DJ, Näbauer M, and Erdmann E.** Alterations of K<sup>+</sup> currents in isolated human ventricular myocytes from patients with terminal heart failure. *Circ Res* 73: 379–385, 1993.
6. **Cherry EM, Greenside HS, and Henriquez CS.** A space-time adaptive method for simulating complex cardiac dynamics. *Phys Rev Lett* 84: 1343–1346, 2000.
7. **Clayton RH, Murray A, and Campbell RW.** Objective features of the surface electrocardiogram during ventricular tachyarrhythmias. *Eur Heart J* 16: 1115–1119, 1995.
8. **Courtemanche M, Ramirez RJ, and Nattel S.** Ionic mechanisms underlying human atrial action potential properties: insights from a mathematical model. *Am J Physiol Heart Circ Physiol* 275: H301–H321, 1998.
9. **Davidenko JM, Pertsov AM, Salomonsz R, Baxter W, and Jalife J.** Stationary and drifting spiral waves of excitation in isolated cardiac muscle. *Nature* 355: 349–351, 1991.
10. **Efimov IR, Krinsky VI, and Jalife J.** Dynamics of rotating vortices in the Beeler-Reuter model of cardiac tissue. *Chaos, Solitons and Fractals* 5: 513–526, 1995.
11. **Efimov IR, Sidorov VY, Cheng Y, and Wollenzier B.** Evidence of 3D scroll waves with ribbon-shaped filament as a mechanism of ventricular tachycardia in the isolated rabbit heart. *J Cardiovasc Electrophysiol* 10: 1452–1462, 1999.
12. **Endresen LP and Skarland N.** Limit cycle oscillations in pacemaker cells. *IEEE Trans Biomed Eng* 47: 1134–1137, 2000.
13. **Fast VG, Efimov IR, and Krinsky VI.** Transition from circular to linear cores in excitable media. *Phys Lett A* 151: 157–161, 1990.
14. **Fenton F and Karma A.** Vortex dynamics in three-dimensional continuous myocardium with fiber rotation: filament instability and fibrillation. *Chaos* 8: 20–47, 1998.
15. **Franz MR, Schaeffer J, Schottler M, Seed WA, and Noble MIM.** Electrical and mechanical restitution of the human heart at different rates of stimulation. *Circ Res* 53: 815–822, 1983.
16. **Frazier DW, Wolf PD, Wharton JM, Tang ASL, Smith WM, and Ideker RE.** Stimulus-induced critical point. Mechanism for electrical induction of reentry in normal canine myocardium. *J Clin Invest* 83: 1039–1052, 1989.
17. **Glass L.** Dynamics of cardiac arrhythmias. *Phys Today* 49: 40–45, 1996.
18. **Gray RA, Pertsov AM, and Jalife J.** Spatial and temporal organization during cardiac fibrillation. *Nature* 392: 75–78, 1998.
19. **Hodgkin AL and Huxley AF.** A quantitative description of membrane current and its application to conduction and excitation in nerve. *J Physiol (Lond)* 117: 500–544, 1952.
20. **Jafri MS, Rice JJ, and Winslow RL.** Cardiac Ca<sup>2+</sup> dynamics: the roles of ryanodine receptor adaptation and sarcoplasmic reticulum load. *Biophys J* 74: 1149–1168, 1998.
21. **Jalife J, Gray RA, Morley GE, and Davidenko JM.** Self-organization and the dynamical nature of ventricular fibrillation. *Chaos* 8: 79–93, 1998.
22. **Jongsma HJ and Wilders R.** Gap junctions in cardiovascular disease. *Circ Res* 86: 1193–1197, 2000.
23. **Koumi S, Backer CL, and Arentzen CE.** Characterization of inwardly rectifying K<sup>+</sup> channel in human cardiac myocytes.

- Alterations in channel behavior in myocytes isolated from patients with idiopathic dilated cardiomyopathy. *Circulation* 92: 164–174, 1995.
24. **Li GR, Feng J, Yue L, and Carrier M.** Transmural heterogeneity of action potentials and  $I_{to1}$  in myocytes isolated from the human right ventricle. *Am J Physiol Heart Circ Physiol* 275: H369–H377, 1998.
  25. **Liu DW, Gintant GA, and Antzelevitch C.** Ionic bases for electrophysiological distinctions among epicardial, midmyocardial, and endocardial myocytes from the free wall of the canine left ventricle. *Circ Res* 72: 671–687, 1993.
  26. **Luo CH and Rudy Y.** A dynamic model of the cardiac ventricular action potential. I. Simulations of ionic currents and concentration changes. *Circ Res* 74: 1071–1096, 1994.
  27. **Main MC, Bryant SM, and Hart G.** Regional differences in action potential characteristics and membrane currents of guinea-pig left ventricular myocytes. *Exp Physiol* 83: 747–761, 1998.
  28. **Morgan JM, Cunningham D, and Rowland E.** Dispersion of monophasic action potential duration: demonstrable in humans after premature ventricular extrastimulation but not in steady state. *J Am Coll Cardiol* 19: 1244–1253, 1992.
  29. **Morgan JM, Cunningham D, and Rowland E.** Electrical restitution in the endocardium of the intact human right ventricle. *Br Heart J* 67: 42–46, 1992.
  30. **Noble D.** A modification of the Hodgkin-Huxley equations applicable to Purkinje fibres action and pacemaker potential. *J Physiol (Lond)* 160: 317–352, 1962.
  31. **Noble D, Varghese A, Kohl P, and Noble P.** Improved guinea-pig ventricular cell model incorporating a diadic space,  $I_{Kr}$  and  $I_{Ks}$ , and length- and tension-dependent processes. *Can J Cardiol* 14: 123–134, 1998.
  32. **Nygren A, Fiset C, Firek L, Clark JW, Lindblad DS, Clark RB, and Giles WR.** Mathematical model of an adult human atrial cell. The role of  $K^+$  currents in repolarization. *Circ Res* 82: 63–81, 1998.
  33. **Plonsey R and Barr RC.** *Bioelectricity: A Quantitative Approach*. New York: Plenum, 1988, p. 213–216.
  34. **Press WH, Teukolsky SA, Vetterling WT, and Flannery BP.** *Numerical Recipes in C: The Art of Scientific Computing*. New York: Cambridge University Press, 1992, p. 870-ff.
  35. **Priebe L and Beuckelmann DJ.** Simulation study of cellular electric properties in heart failure. *Circ Res* 82: 1206–1223, 1998.
  36. **Qu Z and Garfinkel A.** An advanced algorithm for solving partial differential equation in cardiac conduction. *IEEE Trans Biomed Eng* 46: 1166–1168, 1999.
  37. **Qu Z, Weiss J, and Garfinkel A.** Cardiac electrical restitution properties and stability of reentrant spiral waves: a simulation study. *Am J Physiol Heart Circ Physiol* 276: H269–H283, 1999.
  38. **Rice JJ, Jafri MS, and Winslow RL.** Modeling gain and gradedness of  $Ca^{2+}$  release in the functional unit of the cardiac diadic space. *Biophys J* 77: 1871–1884, 1999.
  39. **Rush S and Larsen H.** A practical algorithm for solving dynamic membrane equations. *IEEE Trans Biomed Eng* 25: 389–392, 1978.
  40. **Saumarez RC, Camm AJ, Panagos A, Gill JS, Stewart JT, de Belder MA, Simpson IA, and McKenna WJ.** Ventricular fibrillation in hypertrophic cardiomyopathy is associated with increased fractionation of paced right ventricular electrograms. *Circulation* 86: 467–474, 1992.
  41. **Saumarez RC, Heald S, Gill J, Slade AKB, de Belder MA, Walczak F, Rowland E, Ward DE, and Camm AJ.** Primary ventricular fibrillation is associated with increased paced right ventricular electrogram fractionation. *Circulation* 92: 2565–2571, 1995.
  42. **Volders PG, Sipido KR, Carmeliet E, Spätjens RL, Wellens HJ, and Vos MA.** Repolarizing  $K^+$ -currents  $I_{to1}$  and  $I_{Ks}$  are larger in right than left canine ventricular midmyocardium. *Circulation* 99: 206–210, 1999.
  43. **Witkowski FX, Leon LJ, Penkoske PA, Giles WR, Spano ML, Ditto WL, and Winfree AT.** Spatiotemporal evolution of ventricular fibrillation. *Nature* 392: 78–82, 1998.
  44. **Zemlin CW and Panfilov AV.** Spiral waves in excitable media with negative restitution. *Phys Rev E* 63: 041912, 2001.
  45. **Zygmunt AC, Eddlestone GT, Thomas GP, Nesterenko VV, and Antzelevitch C.** Larger late sodium conductance in M cells contributes to electrical heterogeneity in canine ventricle. *Am J Physiol Heart Circ Physiol* 281: H689–H697, 2001.
  46. **Zygmunt AC, Goodrow RJ, and Antzelevitch C.**  $I_{NaCa}$  contributes to electrical heterogeneity within the canine ventricle. *Am J Physiol Heart Circ Physiol* 278: H1671–H1678, 2000.